Geophysical Journal International

Geophys. J. Int. (2012) **188,** 1071–1087 doi: 10.1111/j.1365-246X.2011.05289.x

Fault geometry, rupture dynamics and ground motion from potential earthquakes on the North Anatolian Fault under the Sea of Marmara

David D. Oglesby[1] and P. Martin Mai[2]

[1]*Department of Earth Sciences, University of California, Riverside,* CA 92521*, USA. E-mail: david.oglesby@ucr.edu*
[2]*Division of Physical Sciences & Engineering, King Abdullah University of Science and Technology, Thuwal* 23955–6900*, Saudi Arabia*

Accepted 2011 November 3. Received 2011 August 29; in original form 2011 February 22

SUMMARY

Using the 3-D finite-element method, we develop dynamic spontaneous rupture models of earthquakes on the North Anatolian Fault system in the Sea of Marmara, Turkey, considering the geometrical complexity of the fault system in this region. We find that the earthquake size, rupture propagation pattern and ground motion all strongly depend on the interplay between the initial (static) regional pre-stress field and the dynamic stress field radiated by the propagating rupture. By testing several nucleation locations, we observe that those far from an oblique normal fault stepover segment (near Istanbul) lead to large through-going rupture on the entire fault system, whereas nucleation locations closer to the stepover segment tend to produce ruptures that die out in the stepover. However, this pattern can change drastically with only a 10° rotation of the regional stress field. Our simulations also reveal that while dynamic unclamping near fault bends can produce a new mode of supershear rupture propagation, this unclamping has a much smaller effect on the speed of the peak in slip velocity along the fault. Finally, we find that the complex fault geometry leads to a very complex and asymmetric pattern of near-fault ground motion, including greatly amplified ground motion on the insides of fault bends. The ground-motion pattern can change significantly with different hypocentres, even beyond the typical effects of directivity. The results of this study may have implications for seismic hazard in this region, for the dynamics and ground motion of geometrically complex faults, and for the interpretation of kinematic inverse rupture models.

Key words: Earthquake dynamics; Earthquake ground motions; Earthquake interaction, forecasting, and prediction; Computational seismology; Continental margins: transform; Dynamics and mechanics of faulting.

1 INTRODUCTION

The North Anatolian Fault (NAF), running across northern Turkey in an east–west direction for ∼1500 km, dominates the seismic hazard in this region, as manifested in the sequence of moderate-to-large earthquakes since 1939 (12 earthquakes with $M > 6.7$; e.g. Ambraseys 1970; Stein *et al.* 1997). The most recent events, the M 7.4 Izmit and the M 7.2 Düzce earthquakes, ruptured the western portion of the NAF in 1999 as it enters the Bay of Izmit, the easternmost part of the Marmara Sea. The western termination of the Izmit earthquake is located only about 40 km southeast of Istanbul (Fig. 1). Towards the western end of the Marmara Sea, the 1912 Saros earthquake (M 7.3) represents the most recent major event, with its eastern extension being still uncertain (Armijo *et al.* 2002; see Fig. 1). Historical earthquakes are reported by Ambraseys & Jackson (2000) to have occurred in 1509 and 1776, with magnitudes in the range 7.2–7.4, most likely located on the northern branch of the NAF as it traverses the Marmara Sea and between the endpoints of the 1912 Saros and the 1999 Izmit earthquakes. The fault system within the Marmara Sea is therefore the only significant portion of the ∼1500 km long NAF that has not ruptured in the past 230 years (Reilinger *et al.* 2000), and a large earthquake is likely to occur on this part of the NAF (Parsons *et al.* 2000; Parsons 2004).

Using probabilistic methods, the seismic hazard in Istanbul has been estimated in recent studies after the 1999 earthquakes (Atakan *et al.* 2002; Erdik *et al.* 2004). Specific ground-motion scenarios based on kinematic models have also been generated (Pulido *et al.* 2004; Sørensen *et al.* 2007). However, the relevant question for seismic hazard assessments is not whether or not an earthquake will occur, but where and how large the next damaging earthquake will be. Hubert-Ferrari *et al*. (2000) suggest the occurrence of two events of equal or larger magnitude than the 1999 Izmit earthquake within the next few decades. In contrast, Le Pichon *et al*. (1999) argue for the possibility of single-event rupture along the entire length of the submarine Marmara Sea fault system. In this context, the detailed fault geometry of the NAF in the Marmara Sea needs to be considered. The NAF splits into several fault branches close to the Düzce rupture zone (Armijo *et al.* 2002): the southern, central, and

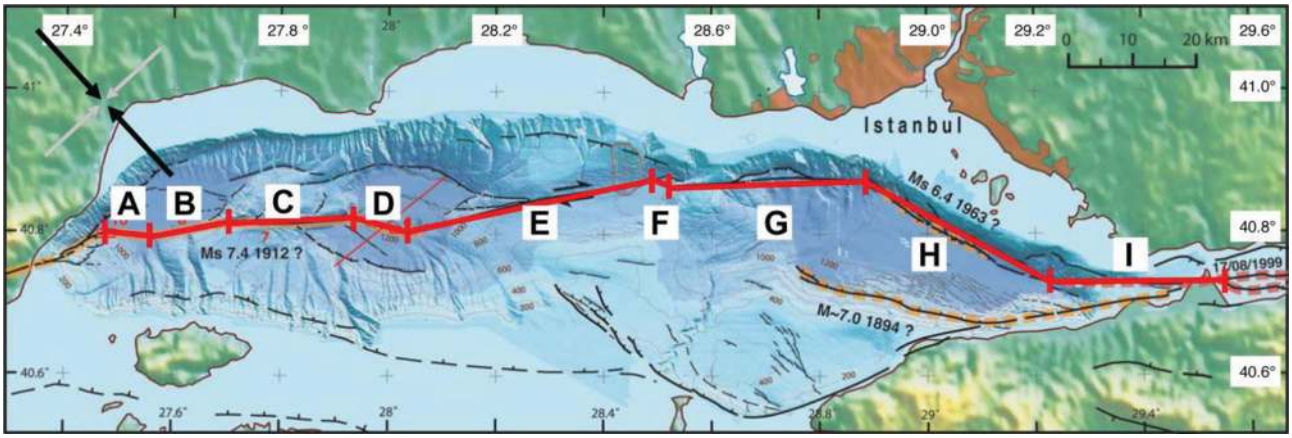

Figure 1. Map view of the North Anatolian Fault (NAF) in the Marmara Sea, with piecewise planar fault geometry overlain. Arrows in upper left denote the orientation of the primary regional stress field (after Armijo *et al.* 2005).

northern NAF. In the Marmara Sea itself, three general fault configurations of currently active faults have been proposed (Parke *et al.* 1999; Okay *et al.* 2000; Imren *et al.* 2001; Le Pichon *et al.* 2001; Armijo *et al.* 2002). These models feature either a single (continuous) strike-slip fault system, or a more complicated geometry with active pull-apart basins. The detailed Marmara Sea fault geometry controls the ability for rupture to propagate along multiple fault segments (Wesnousky 1988; Harris & Day 1999; Muller & Aydin 2004), to thus generate large through-going ruptures, and therefore critically affects the seismic hazard of the city of Istanbul.

For realistic dynamic rupture simulations on the NAF, the properties of the regional stress field need to be considered so that one may resolve the stress components onto the different fault segments. Pinar *et al.* (2003) analysed moment tensors of small-to-moderate size earthquakes in the Marmara Sea to discriminate between different seismotectonic models of the area, as well as to estimate a regional stress tensor. The distribution of fault-plane solutions suggests that the stress field in the eastern part of the Sea of Marmara is relatively homogenous compared to the western part. Pinar *et al.* (2003) identify several shear zones whose locations and sense of motion are explained by a simple deformation model that requires a major E–W striking right-lateral strike-slip fault (the NAF). Their inversion of the orientation of *P*- and *T*-axes of fault-plane solutions results in a regional stress field with maximum compression, σ_1, in the NW–SE direction and minimum compression, σ_3, in the NE–SW direction. However, in the western part of the Sea of Marmara, a more heterogeneous stress field, as indicated by fault-plane solutions, may result from the change in strike of the NAF from nearly E–W to WSW. The corresponding deformation model of an ENE–WSW striking right-lateral strike-slip fault requires a stress field with an ESE-oriented maximum principal stress axis, σ_1, and an NNE-oriented minimum principal stress axis, σ_3. In summary, the NAF in the Marmara Sea experiences an almost horizontal maximum compressive axis σ_1 in the western part, which is rotated by 16° in counter-clockwise sense in the eastern part. The σ_2-axis is almost vertical in the east (pure shear tectonics), whereas it plunges at 36° in the west (transpressive tectonics). Pinar *et al.* (2003) also report changes in the σ_3-axis, being almost horizontal in the east and dipping 49° in the west.

In this study, we investigate rupture dynamics, source sizes and ground-motion patterns for potential earthquakes on the fault system of the NAF in the Marmara Sea using spontaneous dynamic rupture simulations. We consider the 3-D fault configuration proposed by Armijo *et al.* (2002) that best reproduces the observed morphology and vertical structural offsets of a key horizon within the Marmara Sea (Muller & Aydin 2005). To simplify the spatially varying regional stress field, we adopt a uniform regional stress field (σ_1 at 130°, σ_3 at 220°, σ_2 vertical) that is resolved into all fault segments (Fig. 1, Table 1). To account for the spatial changes in the regional stresses and respective uncertainties, we examine the effects when rotating the horizontal principal stresses by 10° clockwise and counter-clockwise. From our suite of dynamic rupture calculations, we then investigate the conditions for and properties of dynamic ruptures on this geometrically complex fault system, their likelihood to generate large through-going earthquakes that pose a severe threat to the city of Istanbul, and the resulting low-frequency ground-motion patterns.

Table 1. Geometrical and stress parameters.

Segment	Length L (km)	Strike φ (degrees)	Normal Stress σ_N (MPa)	Shear Stress σ_S (MPa)	Strength S
A	6.5	96.6	13.03	4.596	0.979
B	13.0	79.4	15.971	4.905	1.414
C	19.1	88.0	14.477	4.973	1.054
D	9.0	105.0	11.786	3.830	1.222
E	39.8	77.8	16.243	4.843	1.523
F	2.4	114	10.760	2.650	2.419
G	36.1	88.6	14.373	4.961	1.040
H	33.6	119.0	10.906	2.306	3.487
I	27.5	88.6	14.373	4.961	1.040

The fault configuration of the NAF within the Marmara Sea also is interesting from a more theoretical point of view, in that it is an example of a geometrically complex fault system that may exemplify many of the attributes that have been studied previously with more generic dynamic faulting models. Many researchers (Segall & Pollard 1980; Harris *et al.* 1991; Harris & Day 1993, 1999; Yamashita & Umeda 1994; Kase & Kuge 1998, 2001; Duan & Oglesby 2006; Oglesby 2008; Oglesby *et al.* 2008) have modelled the behaviour of fault systems with unlinked stepovers, and have found that the ability of rupture to propagate across a stepover depends on (1) the geometrical properties of the stepover (overlap or gap along strike; extensional or compressional stepover), and (2) the details of the stress and slip pattern on the edges of both fault segments. Other work has focused on the effects of fault bends on rupture dynamics (Bouchon & Streiff 1997; Aochi *et al.* 2000, 2002, 2005; Aochi & Fukuyama 2002; Harris *et al.* 2002; Aochi

& Madaraiga 2003; Oglesby & Archuleta 2003; Duan & Oglesby 2005). The results of these studies indicate that rupture propagation at a fault bend depends on an interaction between the initial applied stress field and the dynamic stress field radiated by the rupture front; fault bends may serve as barriers to rupture in some cases, whereas in other cases they may allow through-going rupture.

The NAF in the Marmara Sea, however, is characterized by a large linked fault stepover, just ∼20 km south of Istanbul (Fig. 1; stepover in segments G, H and I). A few studies have examined such linked stepovers. Nielsen & Knopoff (1998) modelled linked stepovers over multiple earthquake cycles using a quasi-static method, and found that these areas could serve as both barriers to rupture and preferred zones of rupture nucleation. Magistrale & Day (1999) modelled the dynamics of thrust faults that are linked by unloaded strike-slip tear faults, and found that the presence of a linking fault greatly increased the potential rupture distance between the thrust faults. Oglesby (2005) performed dynamic models of earthquakes on strike-slip faults with linking dip-slip faults; this general configuration more closely matches the NAF geometry in this work. He found that the results depend on whether the stepover was compressional or extensional: slip on the strike-slip segments in an extensional stepover tended to unclamp the linking normal fault, leading to through-going rupture, whereas the same effect tended to clamp the linking thrust fault in a compressional stepover, thus promoting rupture arrest. He also found that due to the complex dynamic stress interaction between the different segments during the rupture process, the final size of the earthquake is often determined by the location of the hypocentre, and the sequence in which individual segments rupture. Recently, Lozos *et al.* (2011) performed a 2-D dynamic parameter study of strike-slip faults with stepovers and linking strike-slip segments, and found that for large stepover widths the ability of rupture to propagate through a linked stepover was dominated by the static stress field in the stepover region, whereas for short stepover widths it was dominated by the dynamic stress field radiated by fault slip.

The NAF is an ideal test case to see if some of the dynamic effects discovered in the studies above apply in a natural fault system, and whether they have important implications for ground motion in this region. Previously, Oglesby *et al*. (2008) investigated the effect of nucleation location on earthquake size in this region, and noted that a new mode of supershear rupture propagation may result from slip on geometrically complex fault systems. The current work greatly extends this initial work by investigating in detail (1) the effect of stress orientation on earthquake size, (2) the effect of non-planar fault geometry on ground motion and (3) the new mechanism of supershear rupture propagation on non-planar faults. In our study, we use dynamic models to investigate how differences in earthquake sizes, fault slip distributions, rupture propagation patterns and ground motion arise from specific assumptions on the regional stress field and the rupture nucleation location. Although the fault geometry, stress field and other input parameters remain uncertain, experiments with different parametrizations allow us to bracket some of the possible faulting and ground-motion behaviour in this area. For instance, changes in the regional stress direction of $\pm 10^{\circ}$ may significantly alter the rupture properties, which in turn affects the ground motions, which are also sensitive to the overall fault geometry. We also find that the very definition of rupture velocity may need closer examination if dynamic models are to be used in conjunction with kinematic models. Note that other studies (e.g. Pulido *et al.* 2004; Sørensen *et al.* 2007) have previously modelled ground motion in this region with kinematic source models (i.e. with assumed earthquake size, fault slip distributions and rupture timing). Our study is fundamentally different, in that we seek to model the basic physics of the earthquake process. Rather than being specified *a priori*, the earthquake size, slip distribution, rupture timing and the radiated seismic waves are a product of the simulations. As such, our work extends previous ground-motion simulation work in the region as we build physically self-consistent models.

2 METHOD

Our modelling methods and physical setup follow those of Oglesby *et al.* (2008). We use a 3-D explicit finite-element method (Whirley & Engelmann 1993; Oglesby 1999) to model the spontaneous, dynamic rupture of the non-planar NAF. This method has been used to reproduce realistic rupture behaviour in past earthquakes (Oglesby & Day 2001; Oglesby *et al.* 2004), and has been validated as part of the Southern California Earthquake Center/U.S. Geological Survey Dynamic Rupture Code Verification Exercise (Harris *et al.* 2009). The numerical method does not allow fault opening, but when the effective normal stress goes to zero or becomes tensile, the shear stress is set to zero.

Our assumed fault geometry follows a simplified version of that inferred by Armijo *et al.* (2005), shown in map view in Fig. 1; the 3-D fault parametrization (average length of an element edge = 500 m) is portrayed in Fig. 2. We note that for computational ease, the coordinate system of our 3-D fault geometry is rotated 1.4° counterclockwise from the geographic coordinate system. Our computational time step is 8.9×10^{-3} s. Direct inspection of slip-weakening curves indicates that our grid spacing allows us to resolve the physical process of fault strength breakdown. In addition, as detailed later in this work, we performed smaller scale models with higher spatial resolution (grid size = 200 m) and found that our results are robust with respect to grid size. Thus, we verify that our numerical method is resolving the physical processes of interest. With the lowest wave speed being 1.8616 km s^{-1} in our modelling, we estimate that our maximum resolved wave frequency is around 0.4 Hz, assuming 10 grids per wavelength. Fault dips are all vertical, except that of the oblique normal segment H, which has a dip of 70°. Experiments with vertical dip for segment H imply that the results are not very sensitive to dip. The fault system is embedded in a 3-D solid with boundaries far enough from the fault to avoid edge reflections arriving in the domain of interest during the model period. We note that in nature, short segments D and F are likely to be zones of complex deformation, but we parametrize them as short fault segments for simplicity. The faults are embedded in a linearly elastic, isotropic, layered material (Oglesby *et al.* 2008).

We note that our corners are effectively smeared out over roughly one element (500 m) width, so stress build-ups at the fault corners are not singular. The dynamic normal stress in our models eventually reaches zero within one to two elements from the fault edges on segments D, F and H, but this effect simply leads to the shear stress on these points smoothly approaching zero; it does not result in extra seismic radiation or other non-physical behaviour of the nodes in question. A more realistic model would incorporate smoother corners or zones of off-fault damage around the fault corners. We leave unanswered the question of whether fault opening may happen in nature, but due to rock failure and the cutting of secondary faults it is unlikely to be common; we believe that the lack of fault opening in our models does not affect our results significantly.

Our numerical models employ a Coulomb friction law $\tau \leq \mu\sigma_n$, where τ is the frictional stress on the fault, μ is the frictional

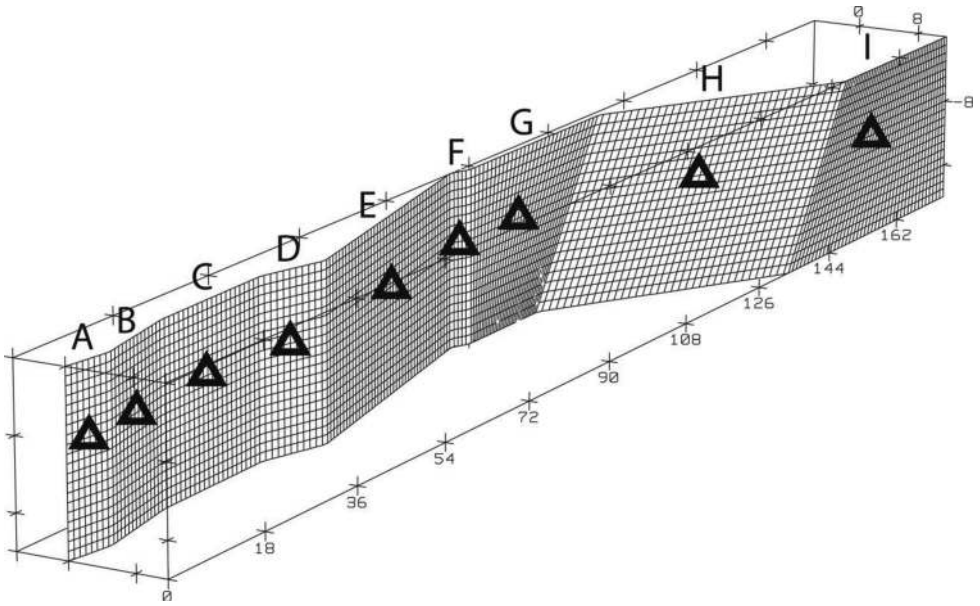

Figure 2. 3-D mesh view of fault geometry; for visual clarity the discretization size shown is double the actual computational discretization size. Locations for which synthetic slip-rate time histories are plotted in the electronic supplement are marked with triangles.

coefficient and σ_n is the normal stress (positive in compression) across the fault. We use a slip-weakening model for the evolution of μ (Ida 1972; Palmer & Rice 1973; Andrews 1976a) with a spatially invariant slip-weakening distance of 0.4 m, a static friction coefficient of 0.6 and a sliding friction coefficient of 0.1. The large drop in frictional coefficient and centimetre-scale slip-weakening distance are motivated by recent experimental/observational (Tsutsumi & Shimamoto 1997; Goldsby & Tullis 2002; Di Toro *et al.* 2004; Han *et al.* 2007) and theoretical/numerical (Andrews 2002; Rice, 2006; Suzuki & Yamashita 2006; Beeler *et al.* 2008; Bizzarri, 2011) work that imply significant fault weakening at high slip rates due to effects such as melting, flash heating and pore fluid pressurization. Our choice of the slip-weakening distance is consistent with the work cited earlier and also is motivated by computational stability concerns. A 50 per cent larger slip-weakening distance results in quite minor changes in the modelled rupture and slip patterns, whereas a 50 per cent smaller slip-weakening distance results in pervasive supershear rupture propagation, which we attribute to a lack of resolution of the slip-weakening process in such a case.

Changes in the compressive normal stress (typical in cases of complex fault geometry) are immediately reflected in this model as changes in the frictional stress. This interplay between the two components of stress will have important implications for the results in this work. The large stress drop with respect to the absolute stresses implied by the above parametrization results in strong dynamic effects in the results, as will be shown later in this work. Rupture nucleation at the selected hypocentre is achieved in our models by artificially increasing the shear stress to the failure level in an expanding circle (rupture velocity $= 3.0$ km s^{-1}) up to a radius of 7 km; beyond this radius, the rupture time is a calculated result of the models. We note that such a large-size nucleation patch is dictated by our assumed stress field: a critical nucleation size for spontaneous nucleation (e.g. Andrews 1976a; Day 1982) applies on each fault segment, and we find that a 7-km large patch is needed to ensure rupture propagation in our models, especially those with nucleation on less-favourable segments. However, additional numerical experiments with a 5.5-km nucleation size on segment B imply that the results beyond the nucleation patch are not very sensitive to the nucleation patch size.

We apply a regional stress field inferred from moment tensor inversions of small- to medium-sized earthquakes (Pinar *et al.* 2003; Oglesby *et al.* 2008), with an orientation depicted in Fig. 1. This regional stress field is then resolved into strike-slip, down-dip and fault-normal stress components on fault segments A–I as a function of each segment's orientation (values of shear and normal stress for each segment are given in Table 1). These values taper linearly to 0.1 of their ambient values between a depth of 3 km and the free surface. We assume a relatively constant effective normal stress (normal stress minus pore fluid pressure) with depth as in many previous faulting models (e.g. Tse & Rice 1986; Rice 1993) to avoid a systematically higher stress drop on deeper parts of the fault (which is not typically observed in real-world earthquakes). This pattern of effective normal stress can be attributed to the pore pressure increasing at lithostatic rather than hydrostratic rates below a certain threshold depth.

In this regional stress field, segments A–G and I are loaded in right-lateral strike-slip direction, whereas segment H is loaded in an oblique normal/right-lateral manner. However, this loading does not constitute an *a priori* constraint in the direction of slip; slip is allowed in any on-fault direction and its direction is a calculated result of the models. We also investigate the effects on source dynamics when rotating the regional stress field by 10° clockwise and counter-clockwise from the above orientation to test the robustness of our results to different assumptions about the tectonic loading. It is important to note that due to the different fault segment orientations, individual fault segments have significantly different initial shear stress and strength. One measure of the differences in stress between the fault segments is the relative fault strength parameter $S = \frac{\tau_{\text{yield}} - \tau_0}{\tau_0 - \tau_{\text{final}}}$ (Andrews 1976b). Under the simplifying assumption that $\tau_{\text{final}} = \mu_{\text{sliding}}\sigma_n$, we calculate the value of S for each segment (listed in Table 1). By this measure, we note that segments such as A, C, G and I are rather favourable for rupture ($S < 1.1$), whereas segments B, E, F and H are less favourable

($S > 1.2$). A static calculation of S may help to explain some aspects of dynamic rupture behaviour. However, slip on one fault segment can strongly affect the stress field of other segments, so the effective value of S on each fault segment changes with time as a result of the interplay between the tectonic pre-stress field and the dynamic stresses.

3 RESULTS

3.1 Stress increments due to slip

Oglesby *et al.* (2008) explored the effect of nucleation location on the ability of rupture to propagate across the stepover segment H. They found that when rupture nucleated far from the stepover segment (i.e. nucleation on segment E or farther west), rupture could propagate across the statically unfavourable oblique segment H. Ruptures that nucleated nearer to or on the stepover segment (i.e. segments G, H or I) arrested prematurely on segment H. The reason for the complex relationship between nucleation location and final earthquake size is the interaction between the tectonic pre-stress field and the dynamic stresses during the earthquake rupture process. Deeper insight into this interaction may be gained by examining the change in shear and normal stress on the fault segments due to a through-going rupture. For nucleation on segment B, the final static stress drop (i.e. final minus initial shear stress) indicates a drop in shear stress over the entire fault system (Fig. 3, top panel) as expected for a through-going rupture. More interesting is the normal stress change (Fig. 3, bottom panel) showing strong positive (clamping) and negative (unclamping) stress variations closely associated with discontinuities in the fault geometry. For example, right-lateral slip on segments G and I has unclamped the edges of segment H, making it more favourable for rupture than if it were to rupture in isolation. This unclamping explains why nucleation on some of the strike-slip segments may produce ruptures that propagate across segment H, even though the tectonic pre-stress (i.e. its S value) would imply that segment H is a barrier to rupture. Conversely, right-lateral slip on segment H has clamped down the adjacent edges of segments G and I. A similar pattern can be seen on (and adjacent to) stepover segments D and F. These segments are dynamically unclamped, but tend to have higher initial S-values due to their orientation ($S = 1.22$ and $S = 2.42$, respectively); rupture propagation on these segments is essentially a contest between the tectonic regional stress, which favours rupture slowing down and terminating, and dynamic unclamping, which favours through-going rupture. This result corroborates findings of Oglesby *et al*. (2008): for the largest and least favourable stepover segment H, nucleation farther away from the stepover segment allows a greater build-up of directivity and dynamic stress waves than nucleation close to segment H. Thus, only earthquakes that nucleate far from segment H will unclamp segment H enough to generate through-going rupture; earthquakes that nucleate adjacent to (or on) segment H do not experience enough of this 'dynamic directivity' effect to overcome the unfavourable tectonic pre-stress field. In these latter cases, rupture terminates quickly when it propagates outside the region of significant dynamic unclamping on segment H.

3.2 Effect of regional stress orientation

As noted earlier, the results of our simulations reflect the interplay between the regional tectonic stress field and the dynamic stress field radiated by the propagating rupture. Since the regional stress

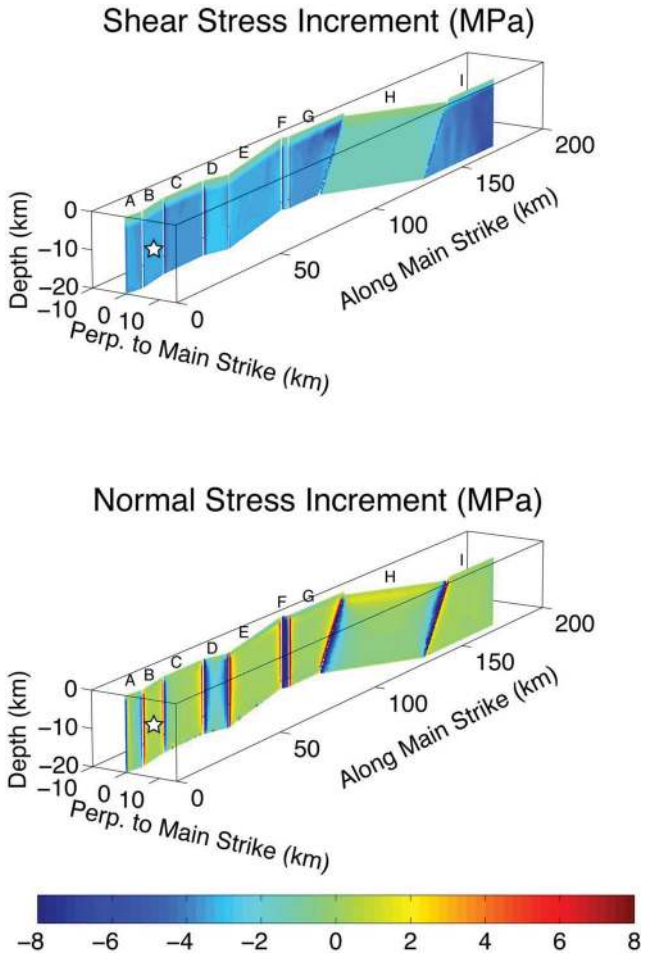

Figure 3. Increments in shear (top panel) and normal (bottom panel) stress on fault system due to an earthquake nucleated on segment B. Strong changes in normal stress are concentrated at the edges of the fault segments. Red denotes clamping and blue denotes unclamping of the fault.

field is not very accurately determined, we examine how variations in the regional stress field affect our modelling. We construct two additional sets of models with different regional stress orientation but the same regional stress amplitude: the first is with the stress field rotated counter-clockwise by 10° with respect to the original stress orientation, and the second is with the stress field rotated 10° clockwise. Final slip patterns for these regional stress orientations are displayed in Fig. 4, with the non-rotated results reproduced from Oglesby *et al.* (2008) in the Supporting Information for comparison.

The effect of rotating the stress field counter-clockwise can be predicted reasonably well by examining Fig. 1. In this rotated stress field, segment H becomes almost parallel to the maximum compressive stress σ_1, thus experiences a very low resolved shear stress, and is therefore quite unfavourable for slip. The dynamic rupture computations corroborate this conjecture, as shown in the final slip distributions (Fig. 4): all simulations, including the B and E nucleation, terminate on segment H under the counter-clockwise rotated stress field. If nucleated on segments G and I, the rupture proceeds an even shorter distance across segment H than in our primary models before dying out.

A 10° clockwise rotation of the regional stress field results in more complicated rupture behaviour than a 10° counter-clockwise rotation. Under this assumption, oblique segment H changes to

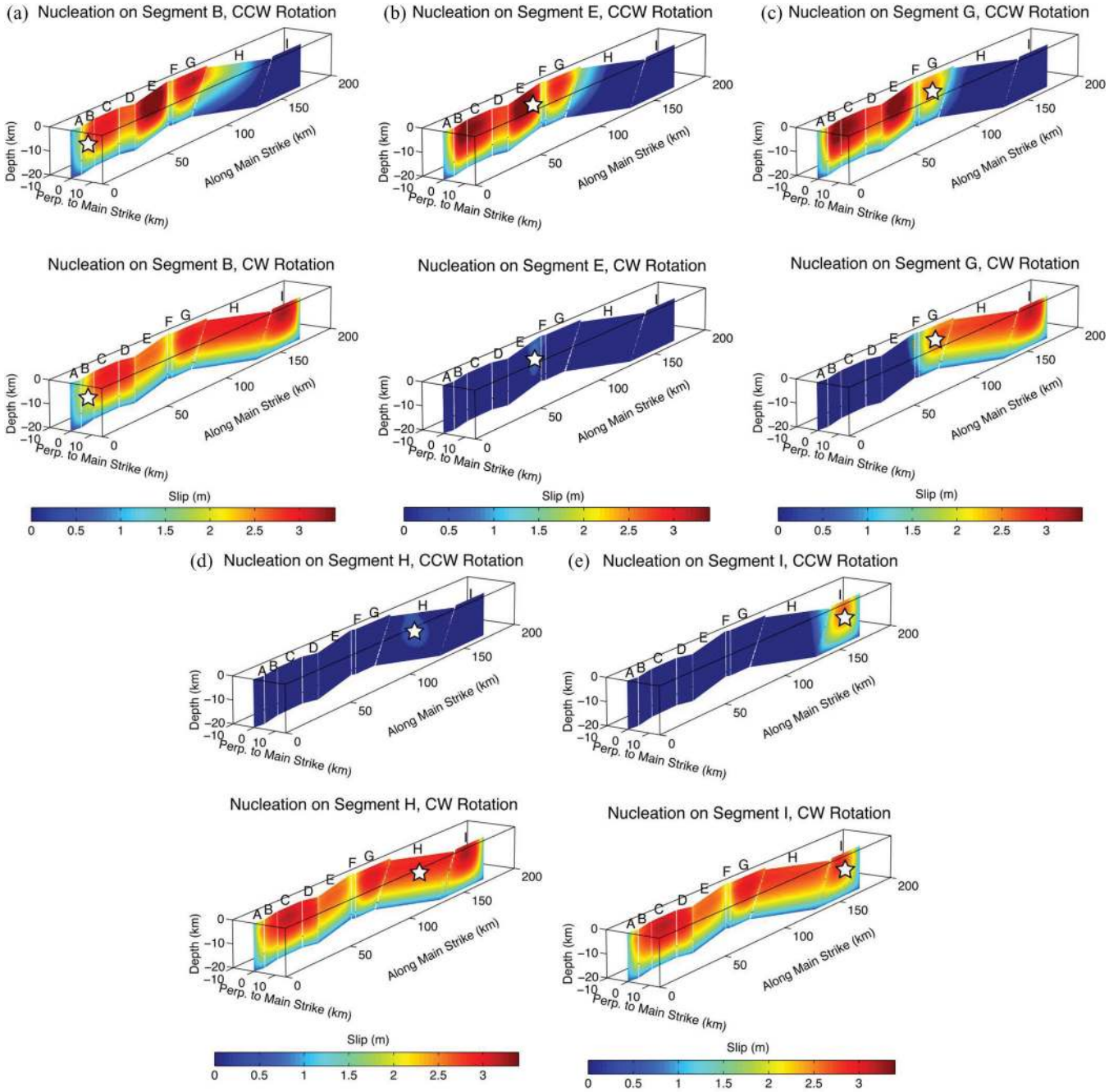

Figure 4. Final slip patterns for earthquakes nucleated on fault segments B (a), E (b), G (c), H (d) and I (e). Results are shown for stress fields rotated counter-clockwise 10° (denoted CCW, top panel) and clockwise 10° (denoted CW, bottom panel) with respect to the primary stress field. The orientation of the regional stress field has a very strong effect on the final earthquake size, and affects the earthquakes differently depending on hypocentre location.

become more favourable for rupture, whereas the main strike-slip segments A, B, C, E, G and I are less favourable. Nucleation on segment B still produces through-going rupture, but the slip distribution has changed qualitatively with respect to the pattern in Oglesby *et al.* (2008), with higher slip on segment H and significantly lower displacements on segment E (which is unfavourable for rupture in this regional stress field). Nucleation on segment E, under our nucleation assumptions, does not produce spontaneous rupture. Nucleation on segment G produces rupture that dies out on segments F and E, but propagates through segment H, onto segment I. Nucleation on segments H and I produces rupture that propagates across the entire fault system. Thus, by rotating the regional stress field only 10° (a value within the uncertainty of the stress orientation estimates), the behaviour of the fault system during dynamic rupture is drastically changed. The role of a barrier is now taken by segment E. Nucleation on segments H and I, which under our initial assumptions in Oglesby *et al.* (2008) produced smaller events, now produce whole-system rupture. Conversely, nucleation on segment E, which previously led to a whole-system event, does not even produce a propagating rupture.

3.3 Temporal evolution of rupture

We now return to an in-depth discussion of our dynamic rupture calculations for the basic (unrotated) regional stress field. More insight into the temporal evolution of rupture propagation, and the dynamic effects that influence it, may be gleaned by examining slip velocity pulses at hypocentral depth (Fig. 5). Nucleation on segment B (Fig. 5a) produces largely unilateral rupture that appears to propagate at a roughly constant rupture velocity until it reaches segment F, where it temporarily speeds up; on segment I the rupture transitions permanently to supershear speed. The sudden rupture acceleration on segment F is due to the dynamic unclamping of this segment, which is otherwise oriented unfavourably for rupture in this stress regime. We note that rupture onto segment G is delayed by approximately 0.5 s because slip on segment F tends to clamp segment G. The acceleration to supershear speed on segment I follows the standard Burridge–Andrews mechanism, with this segment having an S value of less than 1.77 (Andrews 1976b). Nucleation on segment E (Fig. 5b) produces a complex pattern in which the rupture almost dies out at the intersections of segments F and G. We note that while rupture accelerates on segment F for nucleation on segment B, it slows down and almost stops on segment F for nucleation on segment E. Thus, the same segment has opposite effects on rupture propagation for different nucleation locations with the same directivity. This phenomenon may be understood as a combination of static and dynamic effects: segment F is statically unfavourable for rupture, and in the E nucleation case the rupture front has less 'dynamic directivity' than in the B nucleation case. Thus, for E nucleation the shear stress increase and the dynamic unclamping are diminished, and rupture propagation across segment F is more difficult. As in the B nucleation case, slip on segment F tends to clamp segment G, further inhibiting continued rupture propagation. After a delay of approximately 3 s, rupture restarts spontaneously on segment G, and then propagates across the entire fault system. Nucleation on segment G (Fig. 5c) produces a similarly complex rupture pattern. For the same reasons as the E nucleation case, rupture almost dies out at the intersection between segments G and F (although travelling in the opposite direction), while the magnitude of dynamic unclamping is insufficient for rupture to propagate across segment H. Nucleation on segments H and I both produce ruptures that terminate on segment H (not shown for brevity).

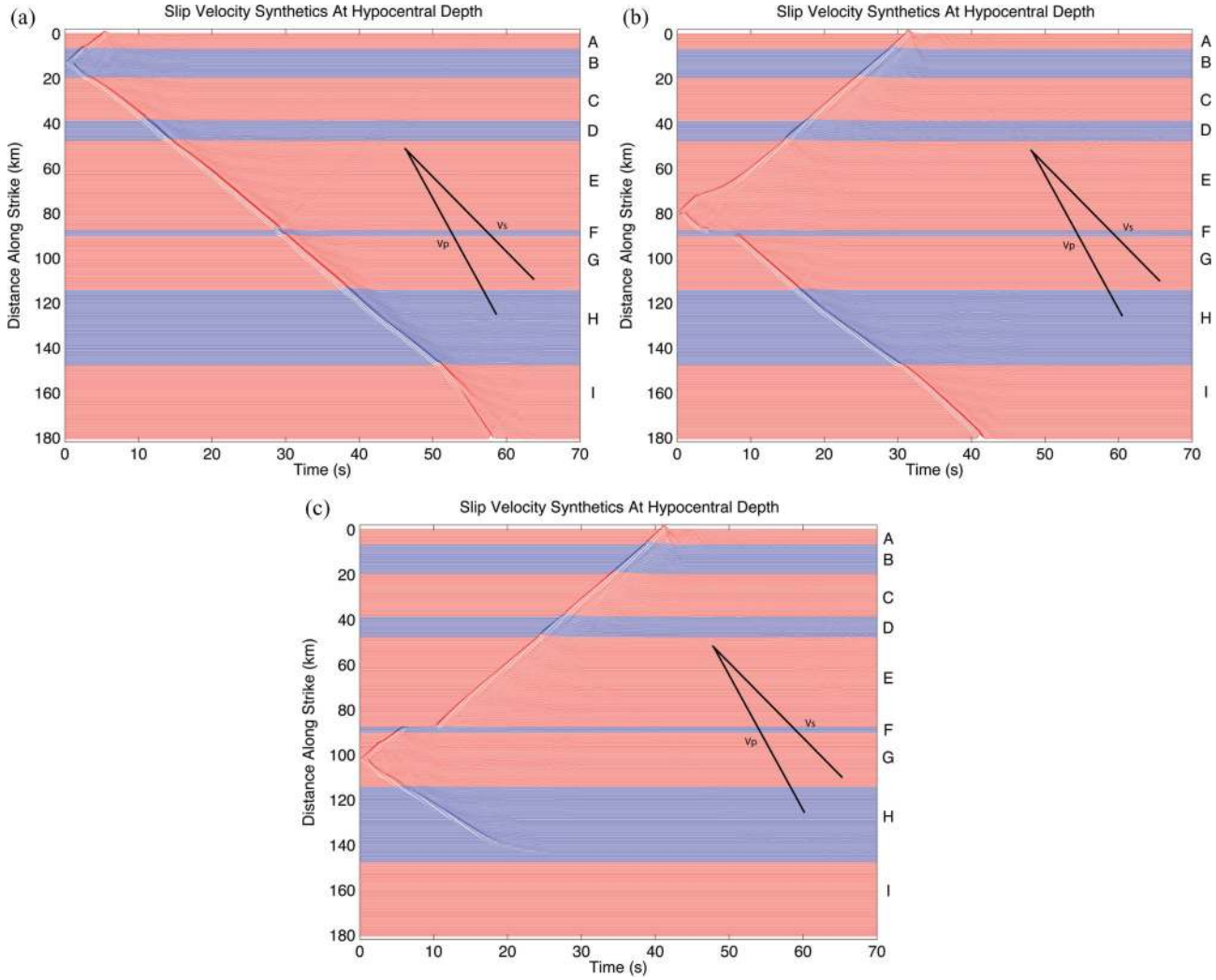

Figure 5. Synthetic slip velocity amplitude (incorporating both strike-slip and dip-slip components) time histories at hypocentral depth ($Z = 8$ km) for points along strike. Different fault segments are labelled and coloured alternately red and blue for clarity. Rupture speeds up and slows down on different fault segments, depending on the nucleation location. The black lines labelled Vp and Vs indicate the moveout of the rupture front propagating at the P- and S-wave speed, respectively, at that depth.

By analysing rupture time and rupture velocity for each point on the fault system, we examine in detail the connection between fault geometry and variations in rupture propagation. Fig. 6 shows rupture time contours and rupture velocity for nucleation on segments B, E and G. Rupture velocity is calculated based on the time at which slip velocity exceeds 1 mm s^{-1} at a given point on the fault. The reciprocal of the spatial gradient of this rupture time distribution is equal to the local rupture velocity. Note that this value need not correspond to any physical quantity in the material, but rather constitutes an apparent rupture speed over the fault plane. Our results are not affected by changing the slip velocity threshold by a factor of two (smaller or larger), implying that the chosen threshold value does not produce artefacts in the rupture velocity distribution. The 'checkerboard' noise in the rupture velocity plots occurs because particle velocities are recorded at an interval of 0.01 s, leading to an apparent quantizing of the rupture velocity; the actual rupture propagation is smooth.

Analysing rupture velocity for nucleation on B (Fig. 6a) reveals an interesting pattern: as noted in Oglesby *et al.* (2008), supershear rupture occurs on the western edges of segments D and F, and the western free surface of H. A new feature in our simulations arises for nucleation on segments E (Fig. 6b) and G (Fig. 6c): the rupture velocity pattern on segment D is spatially reversed (compared to nucleation on B). In these cases, supershear rupture is confined to the eastern edge of segment D. This pattern reversal can be explained if one attributes the supershear rupture propagation to the dynamic unclamping of the segment. When rupture propagates towards segment D from either side, it unclamps the edge of D closest to the previously slipping segment. The unclamped region has significantly lower strength, and thus favours supershear rupture propagation. However, as rupture traverses segment D, it then exits the region of significant unclamping, and reverts to its original slower velocity. This effect can be thought of as an extreme case of the rupture-front acceleration seen in bent fault models of Kase & Day (2006). This mechanism for transition to supershear rupture velocity and its implications will be examined in more detail in the Discussion section.

3.4 Pattern of ground motion

The simulated ground motion from potential earthquakes on this section of the NAF displays many features related to the fault geometry and associated dynamic effects. Fig. 7 compares the simulated peak ground velocity (filtered to 0.25 Hz) of the three components of motion for nucleation on segments B (Fig. 7a) and G (Fig. 7b). The B nucleation case is useful as a general illustration. As expected, ground motion generally increases to the east, reflecting the eastward directivity of the rupture front. The north–south component of motion, normal to the predominant strike of the fault system, measures the largest ground motion, as expected in the case of primarily subshear rupture. However, this familiar pattern is strongly modulated by the fault geometry. Segment H exhibits smaller ground motion than segment G, even though it is farther along strike. Because of the slow rupture propagation around the corner from segments H to I, segment I does not experience a strong directivity effect, leading to smaller near-fault ground motion than on segment G, which has identical values of pre-stress. Additionally, changes in fault strike, which cause the rupture front to accelerate via a change in speed and/or direction, are associated with strong lobes of radiation. This 'corner phase' effect is consistent with isochrone acceleration leading to strong seismic radiation (Bernard & Madariaga 1984; Spudich & Frazer 1984), and also has been noted in some 2-D faulting models (Bouchon & Streiff 1997; Duan & Oglesby 2005; Adda-Bedia & Madariaga 2008). These lobes are particularly visible at segment intersections E–F, F–G, and G–H.

Another striking feature is the asymmetry of ground motion with respect to the northern and southern sides of the fault. In contrast to the symmetric pattern expected for simple planar strike-slip faults, the inside corners of the fault tend to have amplified motion compared to the outside corners. This effect has been noted for fault wall displacements in 2-D faulting models (Davis & Knopoff 1991; Duan & Oglesby 2005), and this work confirms that it is also a strong effect for 3-D ground motion. In more detail, the east–west motion (approximately fault-parallel) and north–south motion (fault-normal) for nucleation on B reveal that asymmetric ground motion are different for the different components of motion: the east–west component exhibits larger ground motion on the south side of segment E and the northeast side of segment H, whereas the opposite is true for the north–south component of motion. The asymmetry of ground motion around segment H is at least partly attributable to the non-vertical dip angle of this segment (e.g. Davis & Knopoff 1991; Oglesby *et al.* 1998), whereas the asymmetry on the other segments arises from non-planarity of the fault system and corresponding seismic radiation at fault kinks (Adda-Bedia & Madariaga 2008).

The net effect of directivity, corner phases radiated at the fault bends and asymmetric particle motion is to produce a complex near-fault peak-motion pattern that becomes more homogeneous farther from the fault due to an averaging effect on radiation from larger areas on the fault system. When comparing the G nucleation case to the B nucleation case (Figs 7b and a), we see some significant differences. The obvious effects are the opposite directions of amplification due to directivity and the lack of strong ground motion near segments H and I, because of rupture dying out on H in the G nucleation case. Another potentially important effect is the spatial variation of ground-motion asymmetry for different directions of rupture propagation. This effect is particularly notable near the small stepover segments D and F. We will examine the case of segment D in more detail (between approximately 35 and 50 km along strike), as shown in the Figs 7(c) and (d), which display the peak horizontal ground velocity (the magnitude of the horizontal velocity vector) for the B and G nucleation cases, respectively. In the B nucleation case (Fig. 7c), rupture approaches from the left (west) edge, and its propagation from segments C to D produces stronger particle motion on the inside of the corner and forward along strike, that is, on the southern side of segment D. A similar effect occurs on the D–E corner, except with the opposite direction of bend. The net effect is to produce stronger ground shaking on the southern side of segment D over most of its length, and higher ground motion on the northern side of segment E. A similar effect occurs on segment F (between approximately 85 and 90 km along strike). When rupture approaches these segments from the opposite direction, such as in the case of G nucleation (Fig. 7d), this effect reverses itself. When the rupture approaches segment D from segment E, it has high directivity and radiates more strongly on the E/D corner, producing higher ground motion on the north side of segment D. A similar effect is seen on the D/C corner, with higher ground motion on the south side of segment C. The ground-motion asymmetry also flips sides on segment F. This effect is most significant for small segments, where the radiation effects from one of the corners is significant over the entire length of the segment. This type of ground-motion variability and asymmetry due to

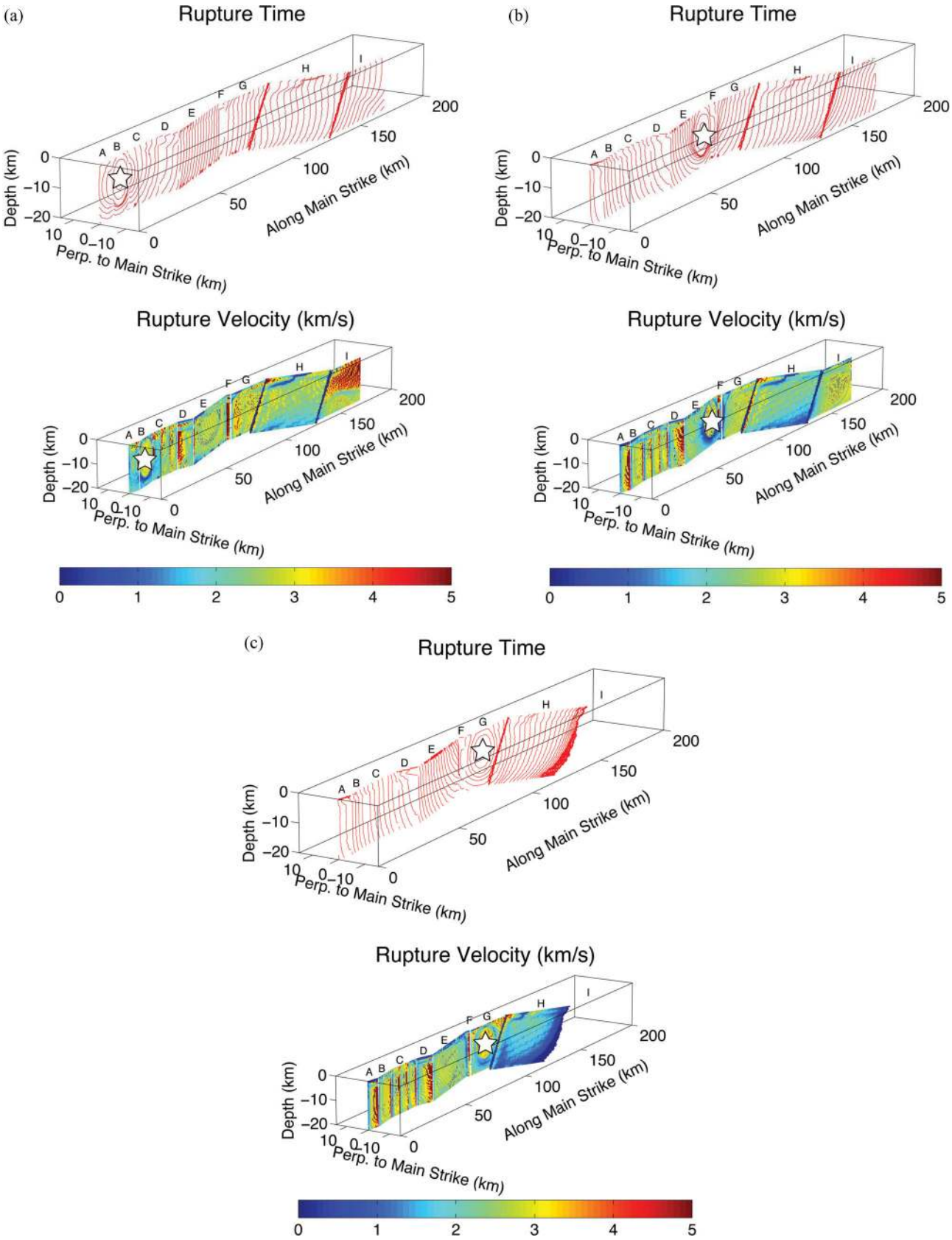

Figure 6. Rupture time contours (top panel) and rupture velocity (bottom panel) for earthquakes nucleated on segment B (a), E (b) and G (c). The location of supershear rupture propagation on segment D changes depending on the nucleation location and hence the direction of rupture propagation.

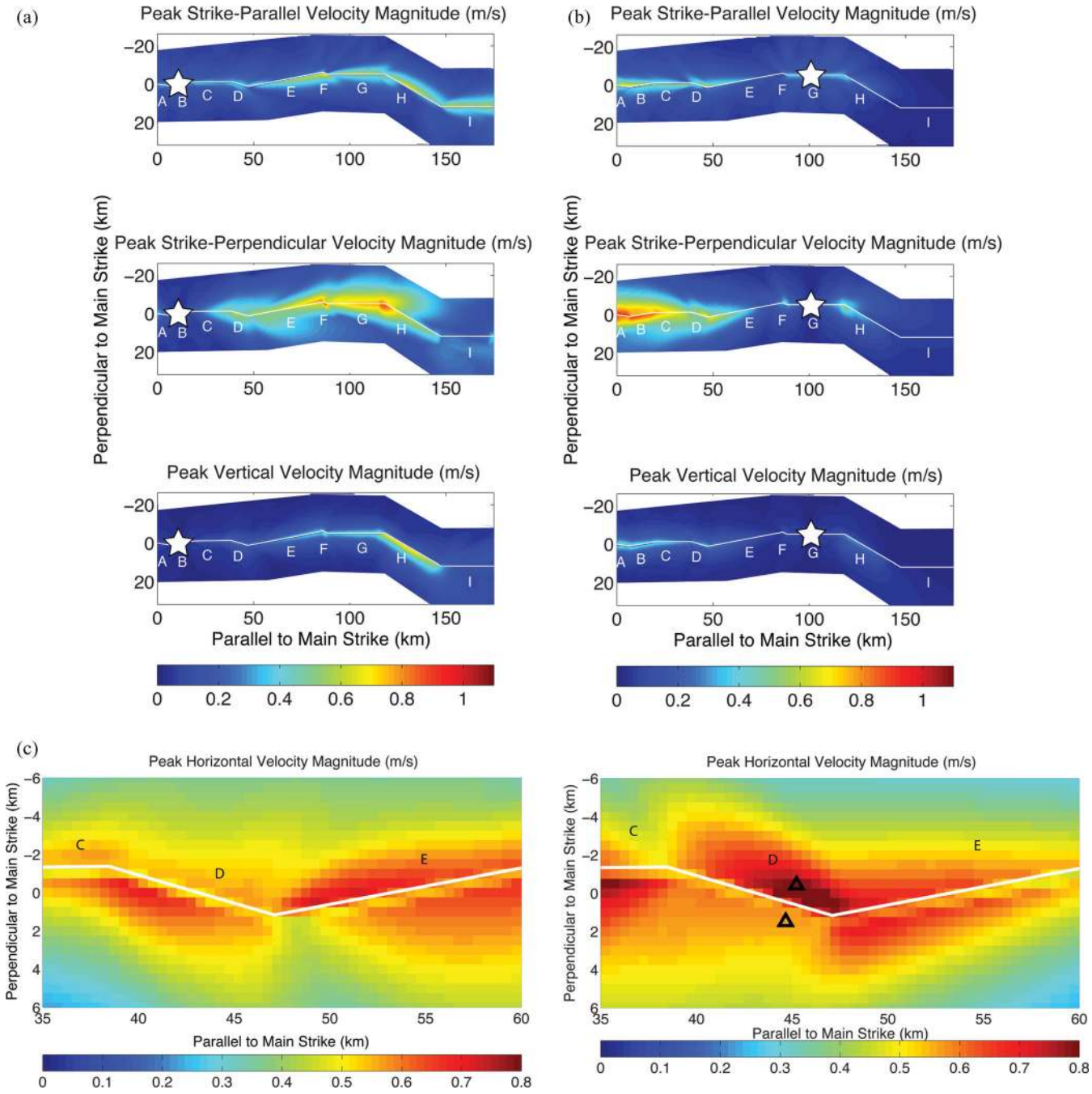

Figure 7. Peak particle velocity amplitude in east–west (top panel), North–South (middle panel) and updown directions (bottom panel) for nucleation on segment B (a) and G (b). North–South direction is perpendicular to the primary fault strike, and thus displays greater effects of directivity. The non-planar fault geometry produces numerous local high-amplitude areas in the ground-motion field, which change significantly for different hypocentre locations. (c) Peak horizontal particle velocity for segments C, D and E for the B nucleation case. (d) Peak horizontal particle velocity for segments C, D and E for the G nucleation case. Triangles indicate locations for synthetic velocity time history plots in electronic supplement. Note that the particle motion asymmetry flips in the north–south direction for different rupture directivity.

complexity in fault geometry is particularly pronounced in the near-field region, and hence is important for earthquake engineering practice in ground-motion prediction.

Finally, we note that typical signatures of supershear rupture propagation (i.e. a Mach cone and fault-parallel motion that is higher than fault-normal motion) are not obvious in our ground-motion maps, even though supershear rupture propagation occurs in our simulations. The only exception is the ground motion near segment I in the B nucleation model (Fig. 7a), where a 'true' (long-lasting) supershear transition takes place. However, there is no notable Mach cone; the supershear rupture manifests itself only as stronger strike-parallel motion than strike-perpendicular. The lack of supershear ground-motion attributes over most of the our model space is likely due to the small areas over which supershear rupture occurs; it also may imply that the propagation speed of the peak slip-rate pulse is more important for ground-motion generation than the propagation

of the rupture front itself. This aspect of the dynamic ruptures will be explored in detail below.

4 DISCUSSION

4.1 Hypocentre location, rupture propagation and earthquake size

The observation that final earthquake size can depend strongly on hypocentre location, even in a uniform regional stress field, has been discussed briefly in a previous study (Oglesby *et al.* 2008). This work corroborates this observation, even under different assumptions about initial fault stress orientation. It also shows that not only do final slip patterns depend on the hypocentre location, but also that the temporal details of the rupture propagation change for different hypocentre locations. In our current models, nucleation on segment B produces relatively smooth rupture propagation across the entire fault system, whereas nucleation on segments E or G produce halting rupture patterns that produce substantially different ground-motion records. In all cases, rupture propagation cannot be predicted solely by the local tectonic pre-stress on each fault segment. Rather, dynamic stress interactions determine whether rupture will propagate or terminate on less statically favourable segments. The findings are in agreement with the observations of Mai *et al.* (2006) who studied the dependency of hypocentre location and slip/stress distribution on the fault using a large number of kinematic finite-fault rupture models. Their work shows that hypocentres are preferentially located close to large slip (high stress) regions on the fault, and they conjectured that otherwise the energetic of ruptures would not allow for a continued growth of the earthquake. Both results argue for a 'holistic' approach to forecast the size of a future earthquake on a given fault system; analysing each segment by itself could lead to incorrect conclusions. Kinematic rupture models for ground-motion simulation that do not account for such dependencies between nucleation point, rupture propagation timing and earthquake size may therefore yield unrealistic ground-motion estimates.

Some of the results in this study have been hinted at in the more generic 3-D work of Oglesby (2005) on linked fault stepovers. Here, we confirm his prediction that dynamic effects lead to interaction between fault segments during rupture, and consequently produce a strong relationship between hypocentre location and final earthquake size. The earlier results, however, argued that dynamic ruptures should easily propagate through extensional stepovers. In contrast, based on different assumptions on initial stress field and geometry, we find that extensional stepovers sometimes may form rather effective barriers to rupture. Analogous effects are explored in more general 2-D models in Lozos *et al.* (2011). Finally, we note that if segments D and F are in fact complex zones of deformation rather than through-going rupture, then the current results may give an upper bound on the likelihood of through-going rupture at these segments. However, dynamic unclamping (and clamping) should still have the same relative effects on rupture propagation.

4.2 Rupture velocity and the supershear transition

Another interesting aspect of rupture propagation in our simulations is the transition to supershear rupture speeds in fault regions that are dynamically unclamped by slip on adjacent fault segments. This mechanism for the supershear transition, initially reported by Oglesby *et al.* (2008), bears further analysis here, as it may represent an extreme example of rupture-front acceleration at fault bends (Kase & Day 2006). Although this supershear transition mechanism appears important in our dynamic simulations, it is not ubiquitous in fault systems with complex fault geometry. By conducting numerical experiments with simpler, two-segment, higher-resolution (200 m element side) models of bending faults under different prestress conditions (Fig. 8), we investigate the conditions under which this supershear transition becomes important. Rupture times and rupture velocity for a model with identical geometry and stress of the corner between faults E and F is shown in Fig. 8(a). As in the B nucleation case, rupture accelerates to supershear speed on the eastern edge of segment II; this effect is associated with the area that is dynamically unclamped by rupture on segment I (compare to Fig. 6a). However, using slightly different values of stress and fault geometry, this effect becomes much less notable. Fig. 8(b) shows the results for a model with a 20° change in strike and shear and normal stresses given in Table 2. Supershear rupture propagation is not evident, indicating that the observed supershear transition mechanism in our Marmara models may not exist in more generic stress and fault geometry configurations; the specific tectonic settings (stress orientations) combined with the structure of the NAF may favour the occurrence of supershear rupture propagation in the current models. We note that while the supershear transition is a result of the dynamic reduction of normal stress, it is not an artefact of zero normal and shear stress near the edges of segments D, F and H. There exist areas over which the rupture is supershear that do not experience zero normal and shear stress, and there exist regions of zero normal stress that do not experience supershear rupture. Also in all cases the onset of zero normal stress is significantly later than the propagation of rupture through these regions.

The spatial variability of rupture velocity for the B nucleation case (Fig. 6) may appear inconsistent with the slip-rate pulses (Fig. 5) that seemingly do not to vary strongly in moveout angle (except on segments F and I). However, closer inspection of Fig. 5 reveals that while the propagation of the maximum slip-rate peak appears rather uniform, the time of initial fault rupture (i.e. the first instance of non-zero slip rate) is less uniform. Thus, it is useful to examine an alternative measure of 'rupture velocity', the propagation speed of the slip-rate peak. This quantity is plotted in Fig. 9 for the B nucleation case, and for the two simplified high-resolution models (displayed in Fig. 8). We note that in all cases, the velocity of the slip-rate peak is more uniform than the propagation speed of the actual rupture front. Furthermore, in cases of supershear rupture propagation, there is a significant difference between the rupture velocity pattern and the slip-rate peak velocity pattern (Compare Fig. 6a with 9a and Fig. 8a with 9b). Conversely, in the cases with no supershear transition (Compare Fig. 8b with 9c), the two quantities are much more similar. Thus, rupture acceleration and deceleration (and in particular, the supershear transition) is not necessarily accompanied by acceleration and deceleration of the peak slip-rate pulse.

This effect is examined in detail in Fig. 10, which zooms into Fig. 5(a) in the area around segment D. Lines connecting the onset of rupture at each point on the fault are marked in red and blue, with an average line connecting the slip-rate peaks marked in green. Also indicated are the *P*- and *S*-wave speeds, with the slopes of the red, blue and green curves marked for comparison. As rupture propagates from segment C onto segment D, the rupture front (red line) reaches supershear speed, by getting farther ahead (1.0 s) of the peak of the slip-rate pulse that propagates at a more uniform speed (green line). As noted earlier, this high rupture velocity is caused by dynamic unclamping of segment D due to slip on segment C. The high rupture-front speed cannot be sustained as the rupture

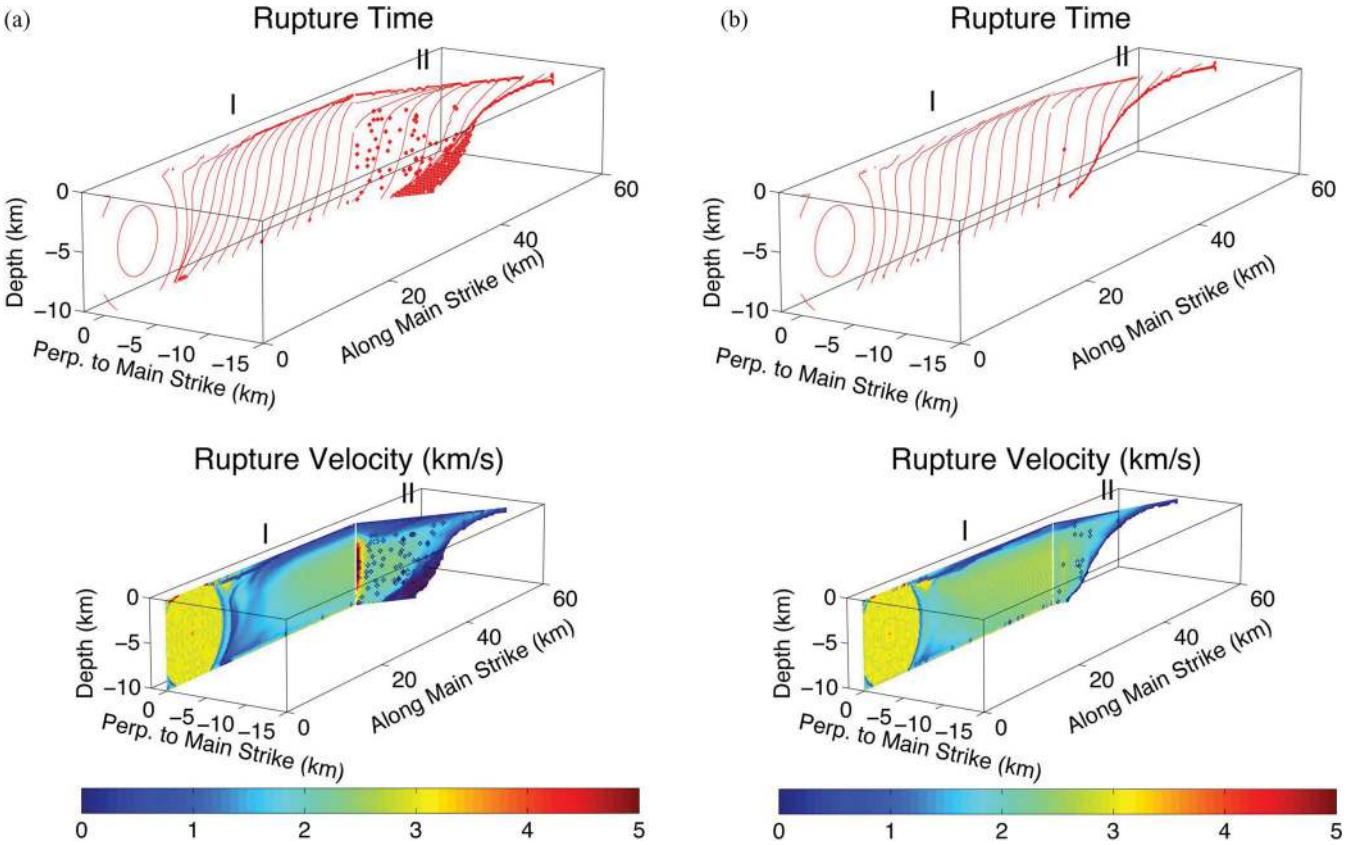

Figure 8. Rupture time contours and rupture velocity for a higher resolution two-segment fault system with (a) fault geometry and stress equivalent to Marmara segments E and F and (b) 20° change in strike with stress pattern shown in Table 2. The geometrically induced supershear transition is evident in the former case, but is absent in the latter.

Table 2. Stress field for high-resolution model with 20° change in strike.

Fault segment	Shear stress (MPa)	Normal stress (MPa)
I	7.6	26.5
II	2.9	22.7

propagates outside of the area of significant dynamic unclamping. The rupture front therefore slows down to subshear speed (blue line), and falls back to be closer (0.7 s) to the slip-rate peak. Note that through all this rupture complexity, the slip-rate peak propagates at almost a constant velocity, indicated by the continuity of the green line connecting peaks in the synthetic slip-rate records.

The above discussion poses two further related questions: (1) Which quantity is more important for seismic radiation: 'rupture velocity' measured by the onset of non-zero slip-rate, or 'velocity of the slip rate peak?' and (2) Which of these quantities can potentially can be resolved from kinematic inversions? We conjecture that the peak of the slip-rate pulse is the strongest source of seismic radiation, and thus the quantity determined by typical slip inversions (e.g. Goto & Sawada 2010). These two measures of rupture velocity may be quite similar in some cases, but quite different in others; in any case, their distinction may be important for a full understanding of rupture propagation and for constructing physics-based kinematic source models for ground-motion simulation (e.g. Mai *et al.* 2001; Guatteri *et al.* 2003; Guatteri *et al.* 2004; Graves & Pitarka 2010; Mai *et al.* 2010; Mena *et al.* 2010). As one example, it may be very difficult to infer the propagation of the true rupture front from a typical kinematic inversion (Goto & Sawada 2010). As another example, consider a kinematic source model based on the rupture time contours from the B nucleation model, and imagine using it to generate ground motion for a potential future earthquake. A typical assumption is to make constant the time between the initial rupture of a point and its peak slip rate. In this case, the 'constructed' velocity of the peak slip-rate pulse would be as heterogeneous as the dynamic rupture velocity of the first non-zero slip-rate. This enhanced variability in rupture propagation speed would likely generate quite different ground motion than the actual dynamic model. Most likely, a kinematic source characterization based on the propagation of the peak slip-rate would represent a more accurate physics-based approximation to the dynamic model.

4.3 Uncertainty in stress and predictability of results

It has long been known that rupture propagation and fault slip distribution depend on the applied stress field. However, it is perhaps unexpected how radically the rupture dynamics change for models in which the initial tectonic stress field is rotated only 10° clockwise. This finding is due to the range of fault orientations in this system; a small rotation of the stress field can bring some segments much closer to failure, whereas other segments are brought much farther from failure. This effect presents significant challenges to the prediction of earthquake size and ground motion for future events, as the local stress field is rarely known within a 10° precision. The problem is even more aggravated when considering other sources

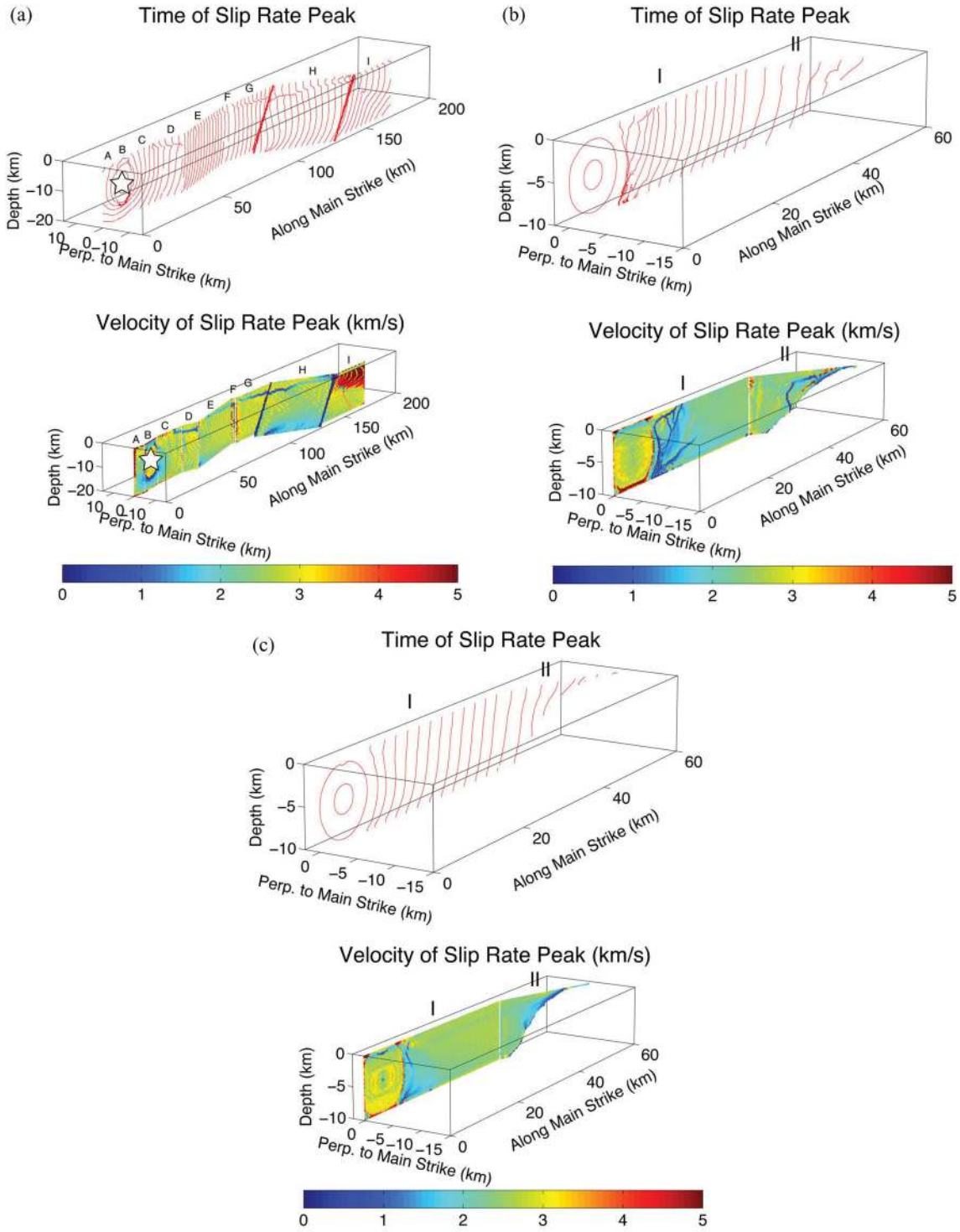

Figure 9. Contours showing timing of peak slip-rate (top panels) and the 'velocity' of the peak slip-rate (bottom panels) for (a) the B nucleation case, (b) the high-resolution model with supershear rupture transition and (c) the high-resolution model with no supershear rupture transition. The 'velocity' of the peak slip-rate pulse is more homogeneous than the rupture velocity for the cases of supershear rupture propagation.

of stress heterogeneity. Our current models make a zeroth-order approximation: the stress field everywhere is simply a regional triaxial field, resolved into the different fault segments. However, natural stress fields are modulated by the effects of prior earthquakes on the fault system (e.g. Tse & Rice 1986; Rice 1993; Nielsen & Knopoff 1998; Lapusta *et al.* 2000; Duan & Oglesby 2005), which can lead to elevated stress levels near the corners of the segments (e.g. Fig. 3). Such stress build-up will be sensitive to the details of the loading history, any potential off-fault relaxation and the detailed geometry of the bend, each of which is estimated only with considerable uncertainty. Furthermore, the stress field near these geometrical discontinuities largely determines whether rupture may propagate through these obstacles or not. Thus, we find ourselves in the uncomfortable position in which the dynamics of the event, including

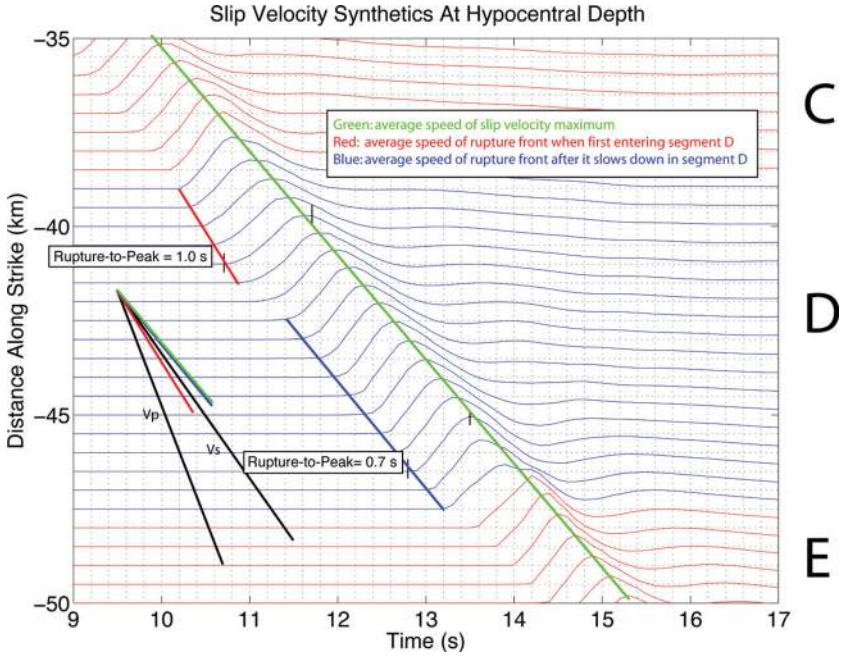

Figure 10. Synthetic slip-rate records for B nucleation case in the vicinity of segment D. Propagation of rupture fronts and slip velocity pulses are marked; see text for discussion. To facilitate the comparison, black lines labelled *Vp* and *Vs* display the moveout of the rupture front propagating at the *P*- and *S*-wave speed, respectively, at that depth.

its final size, may depend critically on the most uncertain aspects of the model.

For example, in our current models, segment H is unfavourably oriented in the regional tectonic stress field, and hence tends to act as a barrier to rupture under a wide range of assumptions. However, unclamping of this segment via slip on the adjacent strike-slip segments may accumulate over multiple earthquake cycles. Eventually, the stress on H (and elsewhere on the fault system) may depart significantly from the regional stress field, and allow through-going rupture on H more easily. Thus, precise knowledge of the regional stress field and its potential rotation close to the fault (Townend & Zoback 2004; Townend 2006) are needed to estimate more reliably the potential properties of future earthquakes on a given fault system. Additionally, more accurate data on fault-zone geometry and material properties near fault segment intersections, as well as true 3-D multicycle earthquake models, may help to reduce some of this uncertainty.

4.4 Implications for ground motion

Previous ground-motion simulations for rupture scenarios on the NAF in the Marmara Sea considered kinematic source models resolved on a simplified two-segment fault geometry (Pulido *et al.* 2004; Sørensen *et al.* 2007). In these configurations, the size and location of high stress-drop asperities are deterministically varied, along with the rupture starting point, assuming one long fault segment extending ∼100 km westward from the major change in strike of the NAF south of Istanbul (between segment G and H in our model setup), and a shorter ∼50 km long segment extending towards the southeast of this intersection. Their hybrid broad-band ground-motion simulations reveal the sensitivity of the spatial distribution of shaking levels to the hypocentre position and asperity locations, explained largely by the relative strength of directivity effects. Because their assumed rupture models are purely kinematic, ground-motion patterns are essentially symmetric with respect to the individual segments for the lower frequencies (i.e. PGV); seismic radiation effects due to rupture dynamics at fault bends are thus not included.

In contrast to the research described earlier, our work describes implications of fault geometry and associated dynamic effects on near-source ground motion. Bouchon & Streiff (1997), Duan & Oglesby (2005) and Adda-Bedia & Madariaga (2008) have noted in 2-D dynamic models that rupture-front acceleration at a fault bend may lead to strong radiation of seismic waves. However, this effect might not necessarily be expected for faults in 3-D because the curved rupture front might not arrive at a fault corner simultaneously, thus leading to a temporal smoothing of the corner effect (more precisely: there would be few points on the surface for which seismic waves from multiple points on the corner arrive simultaneously). However, the lobes of high ground motion around the segment boundaries in our dynamic models indicate that this radiation from fault corners is indeed important in 3-D as well. The most plausible explanation, in case of long strike-slip faults with relatively homogeneous initial stress, is that rupture contours are almost vertical lines once the earthquake has propagated a certain distance, generating a 2-D-like rupture behaviour and arriving at fault corners almost simultaneously. We conjecture that for short faults or faults with highly heterogeneous initial stress (e.g. Ripperger *et al.* 2007; Ripperger *et al.* 2008) these effects may be diminished. However, dynamic rupture simulations as carried out in this study, considering the large-scale geometric features of the fault system, capture only the more coherent low-frequency seismic radiation. Therefore, these geometrical effects on ground motion will be strongly modulated due to other forms of stress heterogeneity leading to complex slip distribution and rupture incoherence. Additionally, wave propagation in 3-D Earth's structure and local site conditions will further complicate the ground-motion pattern, potentially masking the features due to geometric complexity (Olsen

et al. 2008). Higher resolution models, potentially including small-scale stress and geometric inhomogeneity, are necessary to more fully address this question of near-field ground-motion complexity.

Nevertheless, we observe some ground-motion features that probably are more general, including the asymmetry of ground motion on either side of the fault at a corner, and along short segments bounded by double bends (such as segments D and F). Such asymmetric ground motion might contribute to asymmetric off-fault damage in the surrounding rock (Aydin & Du 1995; Duan & Oglesby 2005; Duan & Day 2008), especially in the presence of other mechanisms for preferred rupture orientation, such as loading from a creeping region, or a bimaterial interface (e.g. Dor *et al.* 2006; Shi & Ben-Zion 2006; Brietzke *et al.* 2007; Ampuero & Ben-Zion 2008; Dalguer & Day 2009). If there is no preferred direction of rupture propagation, then some (but not all) of the damage asymmetry may flip sides for ruptures of different directivity, making their effects more difficult to predict ahead of time. However, the inside corners of faults will remain locations of high ground motion.

5 CONCLUSIONS

We have performed spontaneous dynamic rupture simulations for scenario earthquakes on the NAF under a variety of assumptions about hypocentre location and stress orientation. Our simulations clearly show that earthquake size and low-frequency ground motion are sensitive to the particular choices for these physical parameters. New observational data and more accurate modelling methods may help to reduce these uncertainties. Additionally, such uncertainty should be part of a probabilistic seismic hazard analysis for any region around the world with geometrically complex fault systems. In the case of the NAF in the Marmara Sea, through-going rupture is possible under a variety of reasonable assumptions, but may be inhibited under a variety of equally reasonable assumptions. Thus, seismic hazard estimation in the region must fully incorporate both possibilities. Additional work under different assumptions about the fault geometry and other sources of stress heterogeneity may be necessary to fully capture the uncertainty in seismic hazard. From a more theoretical standpoint, our study demonstrates a number of important physical features of earthquakes on geometrically complex fault systems that transcend the specific case of the NAF: (1) the dependence of the final earthquake size on the nucleation location; (2) a new mechanism for supershear rupture propagation and (3) strong effects of the fault geometry on near-source low-frequency ground motion. These effects are all due to the interplay of the local pre-stress field, the fault geometry and the dynamic stress waves generated during the earthquake. These factors, including their epistemic uncertainty, need to be taken into account to reliably estimate ground motion from future earthquakes, both in numerical studies of earthquake rupture dynamics as well as in innovative probabilistic seismic hazard assessment.

ACKNOWLEDGMENTS

The authors gratefully acknowledge K. Atakan and S. Pucci, who contributed greatly to the initial stages of our work in this area. We also gratefully acknowledge R. Armijo, who kindly sent us a map that served as the basis of Fig. 1. We also benefitted from many conversations with L. Dalguer, D. Bowman and J.-P. Ampuero. The paper was greatly improved by the constructive criticism of three anonymous reviewers and the Editor. This work was supported in part by the ETH program for visiting scholars.

REFERENCES

Adda-Bedia, M. & Madariaga, R., 2008. Seismic radiation from a kink on an antiplane fault, *Bull. seism. Soc. Am.,* **98,** 2291–2302.

Ambraseys, N.N., 1970. Some characteristic features of Anatolian Fault Zone, *Tectonophysics,* **9,** 143–165.

Ambraseys, N.N. & Jackson, J.A., 2000. Seismicity of the Sea of Marmara (Turkey) since 1500, *Geophys. J. Int.,* **141,** F1–F6.

Ampuero, J.-P. & Ben-Zion, Y., 2008. Cracks, pulses and macroscopic asymmetry of dynamic rupture on a bimaterial interface with velocity-weakening friction, *Geophys. J. Int.,* **173,** 674–692.

Andrews, D.J., 1976a. Rupture propagation with finite stress in antiplane strain, *J. geophys. Res.,* **81,** 3575–3582.

Andrews, D.J., 1976b. Rupture velocity of plane strain shear cracks, *J. geophys. Res.,* **81,** 5679–5687.

Andrews, D.J., 2002. A fault constitutive relation accounting for thermal pressurization of pore fluid, *J. geophys. Res.,* **107,** doi:10.1029/2002JB001942.

Aochi, H. & Fukuyama, E., 2002. Three-dimensional nonplanar simulation of the 1992 Landers earthquake, *J. geophys. Res.,* **107,** doi:10.1029/2000JB000061.

Aochi, H. & Madaraiga, R., 2003. The 1999 Izmit, Turkey, earthquake: nonplanar fault structure, dynamic rupture process, and strong ground motion, *Bull. seism. Soc. Am.,* **93,** 1249–1266.

Aochi, H., Fukuyama, E. & Matsu'ura, M., 2000. Spontaneous rupture propagation on a non-planar fault in 3-D elastic medium, *Pure appl. Geophys.,* **157,** 2003–2027.

Aochi, H., Fukuyama, E. & Madariaga, R., 2002. Effect of normal stress during rupture propagation along nonplanar faults, *J. geophys. Res.,* **107,** doi:10.1029/2001JB000500.

Aochi, H., Scotti, O. & Berge-Thierry, C., 2005. Dynamic transfer of rupture across differently oriented segments in a complex 3-D fault system, *Geophys. Res. Lett.,* **32,** L21304, doi:21310.21029/22005GL024158.

Armijo, R., Meyer, B., Navarro, S., King, G.C.P. & Barka, A., 2002. Asymmetric slip partitioning in the Sea of Marmara pull-apart: a clue to propagation process of the North Anatolian Fault?, *Terra Nova,* **14,** 80–86.

Armijo, R. *et al*., 2005. Submarine fault scarps in the Sea of Marmara pull-apart (North Anatolian Fault): implications for seismic hazard in Istanbul, *Geochem. Geophys. Geosyst.,* **6,** doi:10.1029/2004GC000896.

Atakan, K., Ojeda, A., Meghraoui, M., Barka, A.A., Erdik, M. & Bodare, A., 2002. Seismic hazard in Istanbul following the 17 August 1999 Izmit and 12 November 1999 Düzce earthquakes, *Bull. seism. Soc. Am.,* **92,** 466–482.

Aydin, A. & Du, Y., 1995. Surface rupture at a fault bend: The 28 June 1992 Landers, California, earthquake, *Bull. seism. Soc. Am.,* **85,** 111–128.

Beeler, N.M., Tullis, T.E. & Goldsby, D.L., 2008. Constitutive relationships and physical basis of fault strength due to flash heating, *J. geophys. Res.,* **113,** B01401, doi:10.1029/02007JB004988.

Bernard, P. & Madariaga, R., 1984. A new asymptotic method for the modeling of near-field accelerograms, *Bull. seism. Soc. Am.,* **74,** 539–557.

Bizzarri, A., 2011. Dynamic seismic ruptures on melting fault zones, *J. geophys. Res.,* **116,** B02310, doi:10.1029/02010JB007724.

Bouchon, M. & Streiff, D., 1997. Propagation of a shear crack on a nonplanar fault: A method of calculation, *Bull. seism. Soc. Am.,* **87,** 61–66.

Brietzke, G.B., Cochard, A. & Igel, H., 2007. Dynamic rupture along bimaterial interfaces in 3D, *Geophys. Res. Lett.,* **34,** L11305, doi:10.1029/12007GL029908.

Dalguer, L.A. & Day, S.M., 2009. Asymmetric rupture of large aspect-ratio faults at bimaterial interface in 3D, *Geophys. Res. Lett.,* **36,** L23307, doi:10.1029/22009GL040303.

Davis, P.M. & Knopoff, L., 1991. The dipping antiplane crack, *Geophys. J. Int.,* **106,** 581–585.

Day, S.M., 1982. Three-dimensional simulation of spontaneous rupture: the effect of nonuniform prestress, *Bull. seism. Soc. Am.,* **72,** 1881–1902.

Di Toro, G., Goldsby, D.L. & Tullis, T.E., 2004. Friction falls toward zero in quartz rock as slip velocity approaches seismic rates, *Nature,* **427,** 436–439.

Dor, O., Ben-Zion, Y., Rockwell, T.K. & Brune, J., 2006. Pulverized rocks in the Mojave section of the San Andreas Fault Zone, *Earth planet. Sci. Lett.,* **245,** 642–654.

Duan, B. & Day, S.M., 2008. Inelastic strain distribution and seismic radiation from rupture of a fault kink, *J. geophys. Res.,* **113,** B12311, doi:10.1029/12008JB005847.

Duan, B. & Oglesby, D.D., 2005. Multicycle dynamics of nonplanar strike-slip faults, *J. geophys. Res.,* **110,** doi:10.1029/2004JB003298.

Duan, B. & Oglesby, D.D., 2006. Heterogeneous fault stresses from previous earthquakes and the effect on dynamics of parallel strike-slip faults, *J. geophys. Res.,* **111,** doi:10.1029/2006JB004138.

Erdik, M., Demircioglu, M., Sesetyan, K., Durukal, E. & Siyahi, B., 2004. Earthquake hazard in Marmara Region, Turkey, *Soil Dyn. Earthq. Eng.,* **24,** 605–631.

Goldsby, D.L. & Tullis, T.E., 2002. Low frictional strength of quartz rocks at subsiesmic slip rates, *Geophys. Res. Lett.,* **29,** 1844, doi:10.1029/2002GL015240.

Goto, H. & Sawada, S., 2010. Trade-offs among dynamic parameters inferred from results of dynamic source inversion, *Bull. seism. Soc. Am.,* **100,** 910–922.

Graves, R.W. & Pitarka, A., 2010. Broadband ground-motion simulation using a hybrid approach, *Bull. seism. Soc. Am.,* **100,** 2095–2123.

Guatteri, M., Mai, P.M. & Beroza, G.C., 2004. A pseudo-dynamic approximation to dynamic rupture models for strong ground motion prediction, *Bull. seism. Soc. Am.,* **94,** 2051–2063.

Guatteri, M., Mai, P.M., Beroza, G.C. & Boatwright, J., 2003. Strong ground-motion prediction from stochastic-dynamic source models, *Bull. seism. Soc. Am.,* **93,** 301–313.

Han, R., Shimamoto, T., Hirose, T., Ree, J.-H. & Ando, J., 2007. Ultralow friction of carbonate faults caused by thermal decomposition, *Science,* **316,** 878–881.

Harris, R.A. & Day, S.M., 1993. Dynamics of fault interaction—parallel strike-slip faults, *J. geophys. Res.,* **98,** 4461–4472.

Harris, R.A. & Day, S.M., 1999. Dynamic 3D simulations of earthquakes on en echelon faults, *Geophys. Res. Lett.,* **26,** 2089–2092.

Harris, R.A., Archuleta, R.J. & Day, S.M., 1991. Fault steps and the dynamic rupture process—2-D numerical simulations of a spontaneously propagating shear fracture, *Geophys. Res. Lett.,* **18,** 893–896.

Harris, R.A., Dolan, J.F., Hartleb, R. & Day, S.M., 2002. The 1999 Izmit, Turkey, earthquake: a 3D dynamic stress transfer model of intraearthquake triggering, *Bull. seism. Soc. Am.,* **92,** 245–255.

Harris, R.A. *et al*., 2009. The SCEC/USGS dynamic earthquake rupture code verification exercise, *Seism. Res. Lett.,* **80,** 119–126.

Hubert-Ferrari, A., Barka, A., Jacques, D., Nalbant, S.S., Meyer, B., Armijo, R., Tapponnier, P. & King, G.C.P., 2000. Seismic hazard in the Marmara Sea region following the 17 August 1999 Izmit earthquake, *Nature,* **404,** 269–273.

Ida, Y., 1972. Cohesive force across the tip of a longitudinal shear crack and Griffith's specific surface energy, *J. geophys. Res.,* **77**, 3796–3805.

Imren, C., Le Pichon, X., Demirbag, E., Ecevitoglu, B. & Görür, N., 2001. The North Anatolian Fault within the Sea of Marmara: a new interpretation based on multi-channel seismic and multi-beam bathymetry data, *Earth planet. Sci. Lett.,* **192,** 595–616.

Kase, Y. & Day, S.M., 2006. Spontaneous rupture processes on a bending fault, *Geophys. Res. Lett.,* **33,** L10302, doi:10.1029/12006GL025870.

Kase, Y. & Kuge, K., 1998. Numerical simulation of spontaneous rupture processes on two non-coplanar faults: the effect of geometry on fault interaction, *Geophys. J. Int.,* **135,** 911–922.

Kase, Y. & Kuge, K., 2001. Rupture propagation beyond fault discontinuities: significance of fault strike and location, *Geophys. J. Int.,* **147,** 330–342.

Lapusta, N., Rice, J.R., Ben-Zion, Y. & Zheng, G.T., 2000. Elastodynamic analysis for slow tectonic loading with spontaneous rupture episodes on faults with rate- and state-dependent friction, *J. geophys. Res.,* **105,** 23 765–23 789.

Le Pichon, X., Taymaz, T. & Sengör, C., 1999. The Marmara fault and the future Istanbul earthquake, in *ITU-IAHS International Conference on the Kocaele Earthquake,* pp. 41–54, eds Karaca, M. & Ural, D. N., Istanbul Tech. Univ., Istanbul.

Le Pichon, X. *et al*., 2001. The active Main Marmara Fault, *Earth planet. Sci. Lett.,* **192,** 595–616.

Lozos, J.C., Oglesby, D.D., Duan, B. & Wesnousky, S.G., 2011. The effects of fault bends on rupture propagation: a geometrical parameter study, *Bull. seism. Soc. Am.,* **101,** 385–398.

Magistrale, H. & Day, S.M., 1999. 3D simulations of multi-segment thrust fault rupture, *Geophys. Res. Lett.,* **26,** 2093–2096.

Mai, P.M., Guatteri, M., Beroza, G.C. & Boatwright, J., 2001. Toward a more physical basis for strong-motion simulation, *Seismol. Res. Lett.,* **72,** 273.

Mai, P.M., Spudich, P. & Boatwright, J., 2006. Hypocenter locations in finite-source rupture models, *Bull. seism. Soc. Am.,* **95,** 965–980.

Mai, P.M., Imperatori, W. & Olsen, K.B., 2010. Hybrid broadband ground-motion simulations: combining long-period deterministic synthetics with high-frequency multiple S-to-S backscattering, *Bull. seism. Soc. Am.,* **100,** 2124–2142, doi:10.1785/0120080194.

Mena, B., Mai, P.M., Olsen, K.B., Purvance, M.D. & Brune, J.N., 2010. Hybrid broadband ground-motion simulation using scattering Green's functions: application to large-magnitude events, *Bull. seism. Soc. Am.,* **100,** 2143–2162, doi:10.1785/0120080318.

Muller, J.R. & Aydin, A., 2004. Rupture progression along discontinuous oblique fault sets: implications for the Karadere rupture segment of the 1999 Izmit earthquake, and future rupture in the Sea of Marmara, *Tectonophysics,* **391,** 283–302.

Muller, J.R. & Aydin, A., 2005. Using mechanical modeling to constrain fault geometries proposed for the northern Marmara Sea, *J. geophys. Res.,* **110,** B03407, doi:10.1029/02004JB003226.

Nielsen, S.B. & Knopoff, L., 1998. The equivalent strength of geometrical barriers to earthquakes, *J. geophys. Res.,* **103,** 9953–9965.

Oglesby, D.D., 1999. Earthquake dynamics on dip-slip faults, *PhD thesis*, University of California, Santa Barbara, CA.

Oglesby, D.D., 2005. The dynamics of strike-slip step-overs with linking dip-slip faults, *Bull. seism. Soc. Am.,* **95,** 1604–1622.

Oglesby, D.D., 2008. Rupture termination and jump on parallel offset faults, *Bull. seism. Soc. Am.,* **98,** 440–447.

Oglesby, D.D. & Archuleta, R.J., 2003. The three-dimensional dynamics of a non-planar thrust fault, *Bull. seism. Soc. Am.,* **93,** 2222–2235.

Oglesby, D.D. & Day, S.M., 2001. Fault geometry and the dynamics of the 1999 Chi-Chi (Taiwan) earthquake, *Bull. seism. Soc. Am.,* **91**, 1099–1111.

Oglesby, D.D., Archuleta, R.J. & Nielsen, S.B., 1998. Earthquakes on dipping faults: the effects of broken symmetry, *Science,* **280**, 1055–1059.

Oglesby, D.D., Dreger, D., Harris, R.A., Ratchkovski, N.A. & Hansen, R., 2004. Inverse kinematic and forward dynamic models of the 2002 Denali Fault Earthquake, Alaska, *Bull. seism. Soc. Am.,* **94,** S214–S233.

Oglesby, D.D., Mai, P.M., Atakan, K. & Pucci, S., 2008. Dynamic models of earthquakes on the North Anatolian fault zone under the Sea of Marmara: effect of hypocenter location, *Geophys. Res. Lett.,* **35,** L18302, doi:10.1029/12008GL035037.

Okay, A.I., Kashlar-Ozcan, A., Imren, C., Boztepe-Guney, A., Demirbag, E. & Kuscu, I., 2000. Active faults and evolving strike-slip basins in the Marmara Sea, northwest Turkey: a multichannel seismic reflection study, *Tectonophysics,* **321,** 189–218.

Olsen, K.B., Day, S.M., Minster, J.B., Cui, Y., Chourasia, A., Okaya, D., Maechling, P. & Jordan, T., 2008. TeraShake2: Spontaneous rupture simulations of M_w 7.7 earthquakes on the southern San Andreas fault, *Bull. seism. Soc. Am.,* **98,** 1162–1185.

Palmer, A.C. & Rice, J.R., 1973. The growth of slip surfaces in the progressive failure of overconsolidated clay, *Proc. R. Soc.,* **A332,** 527–548.

Parke, J.R. *et al*., 1999. Active faults in the Sea of Marmara, western Turkey, imaged by seismic reflection profiles, *Terra Nova,* **11,** 223–227.

Parsons, T., 2004. Recalculated probability of $M \geq 7$ earthquakes beneath the Sea of Marmara, Turkey, *J. geophys. Res.,* **109,** B05304, doi:10.1029/02003JB002667.

Parsons, T., Toda, S., Stein, R.S., Barka, A. & Dieterich, J.H., 2000. Heightened odds of large earthquakes near Istanbul: an interaction based probability calculation, *Science,* **288,** 661–665.

Pinar, A., Kuke, K. & Honkura, Y., 2003. Moment tensor inversion of recent small to moderate sized earthquakes: implications for seismic hazard and active tectonics beneath the Sea of Marmara, *Geophys. J. Int.,* **153,** 133–145.

Pulido, N., Ojeda, A., Atakan, K. & Kubo, T., 2004. Strong ground motion estimation in the Sea of Marmara region (Turkey) based on a scenario earthquake, *Tectonophysics,* **391,** 357–374.

Reilinger, R.E., Toksoz, M.N., McClusky, S. & Barka, A., 2000. 1999 Izmit, Turkey earthquake was no surprise, *GSA Today,* **10,** 1–6.

Rice, J.R., 1993. Spatio-temporal complexity of slip on a fault, *J. geophys. Res.,* **98,** 9885–9907.

Rice, J.R., 2006. Heating and weakening of faults during earthquake slip, *J. geophys. Res.,* **111,** B05311, doi:10.1029/02005JB004006.

Ripperger, J., Ampuero, J.-P., Mai, P.M. & Giardini, D., 2007. Earthquake source characteristics from dynamic rupture with constrained stochastic fault stress, *J. geophys. Res.,* **112,** B0411, doi:10.1029/2006JB004515.

Ripperger, J., Mai, P.M. & Ampuero, J.-P., 2008. Variabilty of near-field ground motion from dynamic earthquake rupture simulations, *Bull. seism. Soc. Am.,* **98,** 1207–1228.

Segall, P. & Pollard, D.D., 1980. Mechanics of discontinuous faults, *J. geophys. Res.,* **85,** 4337–4350.

Shi, Z. & Ben-Zion, Y., 2006. Dynamic rupture on a bimaterial interface governed by slip-weakening friction, *Geophys. J. Int.,* **165,** 469–484.

Sørensen, M.B., Pulido, N. & Atakan, K., 2007. Sensitivity of ground-motion simulations to earthquake source parameters: a case study for Istanbul, Turkey, *Bull. seism. Soc. Am.,* **97,** 881–900.

Spudich, P. & Frazer, L.N., 1984. Use of ray theory to calculate high-frequency radiation from earthquake sources having spatially variable rupture velocity and stress drop, *Bull. seism. Soc. Am.,* **74,** 2061–2082.

Stein, R.S., Barka, A. & Dieterich, J.H., 1997. Progressive failure on the North Anatolian fault since 1939 by earthquake stress triggering, *Geophys. J. Int.,* **128,** 594–604.

Suzuki, T. & Yamashita, T., 2006. Nonlinear thermoporoelastic effects on dynamic earthquake rupture, *J. geophys. Res.,* **111,** B03307, doi:10.1029/02005JB003810.

Townend, J., 2006. What to faults feel? Observational constraints on the stresses acting on seismogenic faults, in *Earthquakes: Radiated Energy and the Physics of Faulting,* pp. 313–327, eds Abercrombie, R., McGarr, A., Kanamori, H. & Di Toro, G., American Geophysical Union, Washington, DC.

Townend, J. & Zoback, M.D., 2004. Regional tectonic stress near the San Andreas fault in central and southern California, *Geophys. Res. Lett.,* **31,** L15S11, doi:10.1029/2003GL018918.

Tse, S.T. & Rice, J.R., 1986. Crustal earthquake instability in relation to the depth variation of frictional slip properties, *J. geophys. Res.,* **91,** 9452–9472.

Tsutsumi, A. & Shimamoto, T., 1997. High-velocity frictional properties of gabbro, *Geophys. Res. Lett.,* **24,** 699–702.

Wesnousky, S.G., 1988. Seismological and structural evolution of strike-slip faults, *Nature,* **335,** 340–343.

Whirley, R.G. & Engelmann, B.E., 1993. DYNA3D: A Nonlinear, Explicit, Three-Dimensional Finite Element Code for Solid and Structural Mechanics—User Manual, UCRL-MA-1107254 Rev. 1, University of California, Lawrence Livermore National Laboratory.

Yamashita, T. & Umeda, Y., 1994. Earthquake rupture complexity due to dynamic nucleation and interaction of subsidiary faults, *Pure appl. Geophys.,* **143,** 89–115.

SUPPORTING INFORMATION

Additional Supporting Information may be found in the online version of this article:

Figure E1. Final slip patterns for earthquakes nucleated on segments B, E, G, H and I for the un-rotated stress pattern, reproduced from Oglesby *et al.* (2008).
Figure E2. Time histories of slip velocity for points given in Table E1 and Fig. 2. Red: strike-slip motion; Blue: dip-slip motion.
Figure E3. Time histories of ground velocity for the two points denoted in Fig. 7(d). Red: north of fault (6.75 km along the strike of segment D, –1 km perpendicular to strike), Blue: south of fault (6.75 km along the strike of segment D, 1 km perpendicular to strike).

Please note: Wiley-Blackwell are not responsible for the content or functionality of any supporting materials supplied by the authors. Any queries (other than missing material) should be directed to the corresponding author for the article.